

A novel humanized PD-1/PD-L1 mouse model permits direct comparison of anti-tumor immunity generated by FDA-approved PD-1 and PD-L1 inhibitors

Whitney Barham

Mayo Clinic

Michelle Hsu

Mayo Clinic

Xin Liu

Mayo Clinic

Susan M. Harrington

Mayo Clinic

Jacob B. Hirdler

Mayo Clinic

Joanina K. Gicobi

Mayo Clinic

XingXing Zhu

Mayo Clinic

Hu Zeng

Mayo Clinic

Kevin D. Pavelko

Mayo Clinic

Yiyi Yan

Mayo Clinic

Aaron S. Mansfield

Mayo Clinic

Haidong Dong (✉ dong.haidong@mayo.edu)

Mayo Clinic

Research Article

Keywords: PD-1, PD-L1, monoclonal antibody, T cell priming, effector T cell

Posted Date: June 13th, 2022

DOI: <https://doi.org/10.21203/rs.3.rs-1659209/v1>

License:  This work is licensed under a Creative Commons Attribution 4.0 International License.

[Read Full License](#)

Abstract

Seven different anti-PD-1 and PD-L1 monoclonal antibodies are now widely used in the US to treat a variety of cancer types, but there have been no clinical trials comparing them directly. Furthermore, because many of these antibodies do not cross react between mouse and human proteins, no preclinical models exist in which to consider these types of questions. Thus, we produced humanized PD-1 and PD-L1 mice in which the extracellular domains of both mouse PD-1 and PD-L1 were replaced with the corresponding human sequences. Using this new model, we sought to compare the strength of the immune response generated by FDA-approved antibodies. To do this, we performed an *in vivo* T cell priming assay in which anti-PD-1/L1 therapies were given at the time of T cell priming against surrogate tumor antigen (OVA), followed by subsequent B16-OVA tumor challenge. We found that anti-PD-1/L1-treated mice exhibited significantly better tumor rejection than controls, although both the control and antibody-treated mice generated comparable numbers of OVA-specific T cells at the time of priming. To determine what could mediate this strong antitumor immune response, we identified the increased production of CX3CR1⁺PD-1⁺CD8⁺ cytotoxic T cells in the anti-PD-1/L1-treated mice, the same subset of effector T cells known to increase in clinical responders to PD-1/L1 therapy. Thus, our model permits the direct comparison of FDA-approved anti-PD-1/L1 monoclonal antibodies and further correlates successful tumor rejection with the level of CX3CR1⁺PD-1⁺CD8⁺ T cells, making this model a critical tool for future studies to optimize and better utilize anti-PD-1/L1 therapeutics.

Introduction

Immune checkpoint blockade therapy (ICB) has transformed the landscape of cancer treatment in the past decade. Due to a relatively manageable toxicity profile and the potential for exceptional results over a long duration, ICB has become the standard of care across many solid tumor types. After initial approvals in 2011 (anti-CTLA-4) and 2014 (anti-PD-1/L1), the number of available options for treatment has continued to increase, particularly therapies targeting PD-1/PD-L1 signaling. There are now four anti-PD-1 antibodies (nivolumab, pembrolizumab, cemiplimab, and dostarlimab) and three anti-PD-L1 antibodies (avelumab, atezolizumab, and durvalumab) approved in the U.S. for indications that stretch across 15 different tumor types^{1,2}.

FDA approval is based on clinical trials comparing each therapeutic to the standard of care, which is often chemotherapy. However, anti-PD-1/L1 antibodies are never directly compared to one another. In some instances, multiple anti-PD-1 and anti-PD-L1 therapies have gained approval for the same indication. For example, nivolumab, pembrolizumab, and atezolizumab are all approved as second-line agents in non-small cell lung cancer. In these cases, decisions on which drug to use are often left to physician preference, as no data exist on which to base these choices. Many would argue that the efficacy of these therapies is equivocal, at least in terms of overall survival. This is somewhat supported by meta-analyses that attempt to mathematically compare the separate trial data³. Nevertheless, each of these biologics has a unique binding site on its target molecule and different modifications to the Fc

region of the antibody^{4,5,6}. Structural modeling has shown that the mechanism by which they bind their targets and the conformation of the molecules once bound differ considerably⁵. The degree to which they each block PD-1 signaling varies⁷. Furthermore, there are reports of durable responses being achieved by one antibody after a similar agent has failed (i.e. nivolumab after pembrolizumab in melanoma and pembrolizumab after atezolizumab in triple-negative breast cancer)^{8,9}. Collectively, this suggests that more careful, direct comparisons of these agents could yield insights that both inform current clinical decisions and lead to better design of the next generation of therapies that target these molecules.

These questions are best addressed within the preclinical space, as conducting copious clinical trials to compare the various anti-PD1/L1 agents is neither feasible nor ethical. Unfortunately, many FDA-approved monoclonal antibodies targeting PD-1 and PD-L1 do not cross react between human and mouse proteins. Consequently, all preclinical studies are performed using anti-mouse antibody clones that strive to recapitulate the anti-human versions but leave us to wonder what differences, if any, may be at play. For example, it has recently been shown that some anti-mouse PD-1 antibody clones may result in unintended depletion of antigen-specific T cells¹⁰. It would be advantageous to be able to compare the genuine FDA-approved biologics head-to-head across various tumor models to determine which would be preferential in certain clinical contexts prior to initiating clinical trials. This would also allow newly developed anti-PD-1/L1 antibody therapeutics or combination strategies to be compared to the currently approved drugs *in vivo* to further refine clinical trial design.

Thus, we developed “HuPD-H1” mice that express humanized PD-1/L1 sequences to permit the use of anti-human PD-1/PD-L1 antibody therapeutics *in vivo*. We first show the characterization of this new model at baseline, ensuring that the chimeric proteins function normally and that they successfully bind to anti-human PD-1/L1 therapeutics. Following characterization, we present our comparative studies, with a particular focus on T cell priming in the context of PD-1/L1 inhibition.

It remains a matter of debate as to precisely where and how anti-PD-1/L1 therapies function to produce successful results in responding patients. Recent studies suggest that at least a portion of the antitumor immune response elicited by these therapies occurs through *de novo* T cell priming in lymphoid organs, perhaps in addition to reinvigorating and expanding exhausted T cell populations at the tumor site.^{11,12,13} However, an effect on priming is not feasible to study within human samples. Patients present with malignant disease, and it cannot be determined whether the treatments given are predominantly working at “time zero” of primary antigen exposure vs. reactivation of dysfunctional T cells in the periphery.

Hence, with our new model, we sought to compare the strength of the immune response generated by FDA-approved antibodies if these antibodies were present during early T cell programming prior to tumor formation. To do this, we combined humanized PD-1/L1 mice with an *in vivo* priming assay in which anti-PD-1/L1 therapies were administered at the time of T cell priming against a surrogate tumor antigen (OVA), followed by subsequent B16-OVA tumor challenge. Tumor rejection vs. formation upon tumor challenge provided a very clear read-out of the strength of the immune reaction produced, which differed among the drugs tested. We then defined the specific population of CD8⁺ T cells that was critical for

enhanced antitumor immunity, a population that was apparent both in our model and in samples from clinical responders. Together, these results demonstrate that HuPD-H1 mice represent a useful tool that will decrease the distance between the preclinical and clinical space and accelerate translational studies to further improve PD-1/L1 therapy.

Methods

Study approval

The Mayo Clinic IACUC approved all animal experiments, and mice were maintained under pathogen-free conditions in the animal facility at Mayo Clinic, Rochester, Minnesota.

HuPD-1 and HuPD-L1 transgenic mice

The appropriate PD-1 and PD-L1 knock-in targeting vectors containing a neomycin (NEO) selection cassette were electroporated into C57BL/6 FLP embryonic stem (ES) cells. ES cells were then screened for uptake of the targeting vector and NEO cassette deletions. Once positive ES cells were identified, they were microinjected into blastocysts, which were then implanted into pseudopregnant foster mice. The resulting chimeras were mated with wild-type C57BL/6 mice, and F1 heterozygotes were identified from their offspring. Ongoing PCR genotyping of the established mouse lines was completed via EconoTaq Plus Green 2X Master Mix and the following primer sequences (annealing temperature of 60 °C):

HuPD-1 FOR 5' – tggctccataccacaagcatgg – 3'

HuPD-1 REV 5' – actctgaagtgtcctgtccgagg – 3'

Wild type band expected at 301bp; if positive for transgene, band expected at 397bp.

HuPD-L1 FOR 5'-aacgtgagagcaagcttatgcttcagg-3'

HuPD-L1 REV 5'-tatccctacaatgccctggcctgg-3'

Wild type band expected at 277bp; if positive for transgene, band expected at 367bp.

Adult mice (2 – 6 months of age) were used in all experimental studies. Approximately equal numbers of male and female mice were used.

Flow cytometry

Cells were stained for flow cytometry assays in FACS buffer (1X PBS, 2 mM EDTA, and 3% FBS). Analysis was completed using a Cytoflex LX (Beckman Coulter) (DAQ Version V2.233, MCB Version: V3.01) running CytExpert software. The antibodies used included anti-mouse CD8-BV421 (clone 53-6.7), anti-mouse CD11a-PerCp/Cy5.5 (clone M17/4), anti-mouse CX3CR1-PE/Cy7 (clone SA011F11), anti-mouse PD-1-APC (clone RMPI30), anti-human PD-1-APC (clone EH12.2H7), anti-mouse CD11c-BV421 (clone N418), anti-mouse CD4-FITC (RM4-5) and anti-mouse CD44-BV711 (IM7), all from BioLegend; iTAg MHC tetramer H-2Kb OVA, SIINFEKL-PE from MBL; anti-mouse B220-SupreBright 600 (RA3-6B2), anti-mouse CD4-eFluor450 (RM4-5), and anti-human PD-L1-PE (clone M1H1), all from Invitrogen; and anti-mouse CD8-APC-Cy7 (53-6.7) and anti-CD62L-PE-Cy7 (MEL-14) from TONBO Biosciences. The detailed gating strategy for the data in **Figure 5** is shown in **Supplemental Figure 1**.

HuPD-1 activated T cells

Spleens from HuPD-1 homozygous mice or wild-type C57BL/6 mice were processed into single cells and plated in complete RPMI medium. Cells were activated with anti-mouse CD3/CD28 Dynabeads (Gibco, 25 μ L beads/1 mL media). After 48 hours of activation, the cells were collected, counted, resuspended in FACS buffer and stained for flow cytometry.

HuPD-L1 BMDM and spleen cell isolation followed by RT-PCR

Mouse bone marrow derived macrophages (BMDMs) were prepared as previously described¹⁴. BMDMs were scraped from plates, counted, and replated on day 6 of maturation. A portion of the cells was treated with 10 μ g/mL LPS (LPS-EB Ultrapure from InvivoGen). Cells were collected after 24 hours of treatment and either (1) stained with anti-human PD-L1-PE (clone M1H1) (Invitrogen) and analyzed via flow cytometry as above or (2) collected in RLT buffer from the Qiagen RNeasy Plus Mini Kit for later RNA isolation.

Whole spleens from homozygous HuPD-L1 mice and C57BL/6 mice were processed into single cells and plated in complete RPMI containing 5 μ g/mL concanavalin A for activation. These cells were collected at 48 hours postactivation in RLT buffer from the Qiagen RNeasy Plus Mini Kit for later RNA isolation.

Cell samples in RLT buffer were processed via the Qiagen RNeasy Plus Mini Kit according to the manufacturer's instructions. Reverse transcription was completed using a SuperScript™ III Reverse

Transcriptase kit (Invitrogen), followed by PCR with Platinum PCR Supermix High Fidelity (Invitrogen). The following primers were used with an annealing temperature of 55 °C and 35 total PCR cycles:

Mouse PD-L1 FOR 5'-ACCTTAAGCCTCAGCACAGC-3'

Mouse PD-L1 REV 5'-GTGGCTGGATCCACGGAAAT-3'

Human PD-L1 FOR 5'-CCTGGCTGCACTAATTGTCT-3'

Human PD-L1 REV 5'-CAGATGACTTCGGCCTTGGG-3'

cDNA was separated on a 2% gel and visualized under UV light.

Dendritic cell isolation

HuPD-H1 mice were given a single i.p. injection of 0.5 mg of OVA protein (Sigma) and 50 µg of poly I:C (Novus). Untreated HuPD-H1 mice were used as controls. Spleens were harvested 20 hours later from both treated and untreated mice, and dendritic cells (DCs) were isolated from total spleen cells using the Easy Sep Mouse Pan-DC enrichment kit (StemCell Technologies). DCs were then resuspended in FACS buffer and blocked with anti-mouse CD16/32 (clone 93) (Biolegend), followed by staining for flow cytometry with anti-mouse CD11c-BV421 (clone N418) (Biolegend) and anti-human PD-L1-APC (clone M1H1) (Invitrogen). One hundred micrograms each of atezolizumab and avelumab was labeled with the Alexa Fluor™ 647 Antibody Labeling Kit (Invitrogen) and used for flow cytometry staining. Flow cytometry analysis was completed as above.

Receptor Occupancy

HuPD-H1 mice were given a single i.p. injection of 0.5 mg of OVA protein (Sigma) and 50 µg of poly I:C (Novus). On day 7 postimmunization, pembrolizumab conjugated to AF647 was injected (i.p.) into HuPD-H1 mice. Spleens were collected 24 hours later and processed into single cells. A portion of cells was analyzed for AF647 staining without further modification, while a second portion of cells from the same mouse was saturated with labeled pembrolizumab prior to flow analysis (20 µg/mL pembro-AF647 for 30 minutes at 4 °C, followed by washing with FACS buffer). All cells were stained with anti-mouse CD8-BV421 (clone 53-6.7) (BioLegend), and flow cytometry was completed as above. Receptor occupancy was calculated using the following formula:

(% of total CD8⁺ cells that were pembro-AF647⁺ after *in vivo* injection) divided by

(% of total CD8⁺ cells that were pembro-AF647⁺ after *ex vivo* saturation)

x 100

= Receptor occupancy

Cell Lines

MC-38 wild-type and MC-38PD-L1KO cells were a kind gift from Dr. Yang-Xin Fu¹⁵. Human PD-L1 was introduced using a pcDNA3.1 vector with full-length cDNA of human PD-L1^{16,17}. MC38huPD-L1 cells were cultured in complete RPMI under selection with G4-18 (0.4 mg/mL). B16-OVA cells were a kind gift from Dr. Richard Vile, Mayo Clinic, and were cultured in complete RPMI under selection with G4-18 (0.8 mg/mL). B16F10 cells were ordered from ATCC. All cell lines were assessed for mycoplasma contamination via PCR and were negative.

Tumor experiments:

For the MC38huPD-L1 study, 0.75×10^6 MC38huPD-L1 cells suspended in 100 μ L of PBS were injected subcutaneously into the right flanks of HuPD-H1 mice. Mice were checked for tumor growth starting on day 7 after tumor injection and randomized into treatment groups such that each group had a similar average tumor size at start. Perpendicular tumor measurements were taken twice per week by calipers. Drug treatments included 100 μ g each of atezolizumab, pembrolizumab, or avelumab injected i.p. in 200 μ L of PBS on days 7, 10, 13, 16, and 20 post tumor injection. Two hundred microliters of PBS was injected as a control. Mice were euthanized if tumors grew beyond 200 mm² or if tumors became ulcerated. All remaining mice were euthanized on day 55 post-tumor injection.

For all priming experiments, each mouse received a one-time injection (i.p.) of 0.5 mg of OVA protein (Sigma) and 50 μ g of poly I:C (Novus) in a total volume of 200 μ L. Drug treatments included 100 μ g each of atezolizumab, pembrolizumab, nivolumab, or avelumab injected i.p. Initial tumor challenge was performed with 1×10^6 B16-OVA tumor cells injected s.c. into the right flank. For rechallenge experiments, mice with no measurable tumors on day 19 post original B16-OVA injection were rechallenged with 1×10^6 B16-OVA cells in the left flank and 1×10^6 B16F10 cells near the right shoulder. All remaining mice were euthanized at day 14 post-rechallenge. To achieve CD8⁺ T cell depletion, 500 μ g of anti-CD8 (clone 2.43) (BioXcell) was injected (i.p.) on day -1 of the study, followed by 200 μ g of anti-CD8 on subsequent injections (days 3, 10, and 17).

CyTOF analysis

HuPDH-1 mice (n=6) received a one-time injection (i.p.) of 0.5 mg of OVA protein (Sigma) and 50 µg of poly I:C (Novus) on day 0 of the experiment. In addition, mice received either avelumab (100 µg) or an equivalent volume of PBS injections on days -1, 1, and 3. All mice were given a tumor challenge with 1×10^6 B16-OVA tumor cells, injected s.c. into the right flank on day 7. Spleens were then collected on day 10 and processed into single cells in complete RPMI media (Corning). Cells from each sample were blocked with 1 µg anti-mouse Fc block (BD Biosciences) for 10 minutes at room temperature followed by staining with a cocktail of antibodies for the T cell panel (**Supplemental Table 1**). Surface marker staining was performed in cell staining buffers (Fluidigm) at room temperature for 30 minutes. Intracellular cytokine staining was performed using a Cytofix/Cytoperm Kit (BD Biosciences) per the manufacturer's protocol. Upon completion of staining, cells were stored in fresh 1% methanol-free formaldehyde in PBS (Thermo Fisher Scientific) until the day of data collection. All events were acquired on a Helios mass cytometer (Fluidigm). Randomization, bead normalization, and bead removal of the data collected were performed using CyTOF software (Fluidigm). Individual FCS files were exported for analysis and uploaded to the Cytobank software platform (Beckman Coulter) for subsequent analysis. Initial gating via Cytobank used ^{191}Ir and ^{193}Ir DNA intercalators as well as the event length parameter to discern intact singlets from debris and cell aggregates. Live/dead staining was then used to identify live intact singlets. Then, all CD45^+ cells were gated, followed by gating for $\text{CD3}^+\text{CD8}^+$ double-positive cells. This population ($\text{CD3}^+\text{CD8}^+$) was then used for subsequent viSNE and CITRUS analysis as detailed below.

viSNE/t-SNE (t-distributed stochastic neighbor embedding) is a nonlinear dimensionality reduction algorithm developed based on Stochastic Neighbor Embedding and available in Cytobank. It uses probability value rather than distance to model the similarity between data points¹⁸. For viSNE analysis, files were categorized into either avelumab-treated (n=3) or PBS-treated (n=3) groups. Twenty-eight markers from the T cell panel were used to build the map, including CX3CR1, CD39, Eomes, TCR β , Tcf1, CD69, Gata3, ROR γ T, Tim3, IRF4, CD25, CD28, BATF, PD-1, CD11a, CD62L, CD4, CD73, CD38, CD272, CD161NK1.1, CD11b, Fas, CD223, iNos, CD44, CD11c, and CD45. A total of 173,784 events were extracted by the algorithm using equal sampling of 28,964 events per .FCS file. A total of 2,000 iterations were completed with a final KL divergence of 4.79075. Once maps were generated, the relative expression level of each marker of interest could be visualized.

Following viSNE analysis, cell subset abundance and functional marker expression were compared using the CITRUS algorithm in Cytobank^{19, 20}. As noted by Ben-Shaanan et al., this analysis starts with a pool of single-cell events and iteratively hierarchically clusters them based on the similarity of the expression of subsets of the measured channels. This produces overlapping clusters, with the largest cluster being one encompassing all of the sampled events. The pooled data set is then split back into its constitutive samples, and the relative abundance of cells in each cluster is computed. We used the SAM algorithm

with a false discovery rate (FDR) of 5% ($P < 0.05$) to determine if any of the computed clusters of CD3⁺CD8⁺ cells were significantly increased or decreased in abundance when comparing avelumab vs. PBS-treated mice. A total of 20,000 events were sampled per file (total of 120,000 events clustered) with a minimum cluster size of 3%. SAM analysis was run three separate times to ensure reproducibility of the results. Cluster #11994 was significantly increased in the avelumab-treated mice in each iteration.

General statistical analysis

The statistical tests performed and the exact “n” included in each experiment are stated within the figure legends. Statistical analysis included the Gehan-Breslow-Wilcoxon test for survival, unpaired t test to determine differences between two groups, and log-rank (Mantel Cox) test to compare time to tumor formation. Statistical analysis was performed using GraphPad Prism v8.4.3 or later, with the exception of Figure 5E, which was completed using Cytobank software, as above. In graphs, bar height represents the mean, and error bars are the standard error of the mean, unless otherwise stated. The number of samples for each group was empirically chosen based on knowledge of intragroup variation and expected effect size. No statistical methods were used to predetermine sample sizes. No data were excluded from the analysis. All experiments were repeatable, and the observations were reproducible. Individual tumor growth curves are shown throughout the manuscript to allow the reader to assess variability among individual mice in each experiment. To minimize potential confounders in all experiments, mice of different treatment groups were cohoused (mixed among the cages), and the order in which the cages received treatments was varied each week. Lab members performing caliper measurements of mouse tumors were blinded to the treatment group.

Results

Generation and characterization of humanized PD-1 and PD-L1 mice

To generate mice expressing PD-1 and PD-L1 proteins that could be bound by FDA-approved humanized monoclonal antibodies, we used homologous recombination in embryonic stem cells to replace the endogenous mouse exons coding for the extracellular domains of PD-1 (exons 2 and 3) or PD-L1 (exons 3 and 4) with the coding sequence for the corresponding human exons (**Figure 1A, B**). The remaining mouse exons of each gene were kept intact to ensure normal downstream signals from each molecule within the cytoplasm. These mice were generated on the immunocompetent C57BL/6 background and appeared grossly normal, with no apparent differences in birth rate, growth curves, fertility, or lifespan between the knock-in mice and wild-type C57BL/6 controls.

To evaluate whether our genetic knock-in approach resulted in appropriately expressed and localized proteins, cells from the spleens of C57BL/6 wild-type mice or mice homozygous for the human PD-1 knock-in (“HuPD-1”) were plated and activated with anti-mouse CD3/CD28 beads for 48 hours to drive PD-1 expression on CD8⁺ T cells. Cells were then stained with commercial flow cytometry antibodies specific for either the mouse or human PD-1 sequence. As expected, PD-1 on wild-type mouse CD8⁺ T

cells was detected exclusively by the anti-mouse specific PD-1 clone, while PD-1 on HuPD-1 CD8⁺ T cells was detected only by the anti-human specific PD-1 antibody clone (**Figure 1C, D**).

Because PD-L1 expression is typically very low in normal tissues at baseline but can be induced on monocytes and macrophages, we assessed the expression of the chimeric PD-L1 gene in either bone marrow-derived macrophages (BMDMs) treated with lipopolysaccharide (LPS) or cells from whole spleens treated with concanavalin A (ConA). Using primers specific for the extracellular portions of either mouse or human PD-L1, we detected the mouse version of PD-L1 mRNA in cells from wild-type mice and the humanized version of PD-L1 mRNA in “HuPD-L1” mice via RT-PCR (**Figure 1E**). In addition, flow cytometry revealed both baseline and increased surface expression of humanized PD-L1 on BMDMs after LPS treatment, confirming that the chimeric protein is appropriately upregulated by an inflammatory stimulus (**Figure 1F**).

Next, we produced double knock-in mice that were homozygous for both HuPD-1 and HuPD-L1 sequences. These mice were used in all subsequent experiments and are referred to as “HuPD-H1.” We compared HuPD-H1 mice with wild-type C57BL/6 controls to ensure that there were no differences in the relative proportions of lymphocyte subsets at baseline. The relative proportions of T cells (CD4⁺, CD8⁺) and B cells (B220⁺) were normal in spleens from HuPD-H1 mice, and the relative proportions of naïve (CD62L⁺ CD44⁻), central memory (CD62L⁺ CD44⁺) and effector (CD62L⁻ CD44⁺) T cell populations were also equivalent to those in wild-type mouse spleens (**Figure 2A**).

Then, we sought to ensure that FDA-approved anti-human PD-L1 therapies could bind to chimeric PD-L1 protein expressed by HuPD-H1 mice. To test this hypothesis, we injected HuPD-H1 mice with OVA/poly I:C to increase PD-L1 expression in DCs (vs. untreated littermates) and then isolated DCs from the spleens 20 hours later. Atezolizumab (atezo) and avelumab (avelu) were directly conjugated to Alexa Fluor 647 (AF647) so that they could be detected via flow cytometry. The commercial flow cytometry antibody clone M1H1, which is typically used to detect PD-L1 on human cells, was used as a positive control. The results showed that atezolizumab and avelumab were both able to bind PD-L1 on HuPD-H1 DCs (**Figure 2B**). As expected, there was an increased level of PD-L1 staining on DCs isolated from mice treated with Poly I:C/OVA compared to untreated mice, confirming the specificity of antibody-PD-L1 binding (**Figure 2B**).

We next considered whether FDA-approved anti-PD-1 therapy could bind to PD-1 in the HuPD-H1 model and assessed this *in vivo* via a pharmacologic assay known as “receptor occupancy.” Mice were first given an injection of OVA protein combined with poly I:C to stimulate an immune reaction. On day 7 postimmunization, pembrolizumab conjugated to AF647 was injected into HuPD-H1 mice (intraperitoneal injection; i.p.) at varying concentrations. Spleens were collected 24 hours later, and the percentage of CD8⁺ T cells bound by pembrolizumab was quantified by flow cytometry. This was further compared to a portion of cells from the same spleens that were saturated with labeled pembrolizumab *ex vivo*, allowing us to quantify the maximum amount of PD-1 that could be bound vs. what had been bound *in vivo*. In our model, PD-1 receptor occupancy on CD8⁺ T cells ranged from 67.1% to 81.3% and was not dose

dependent, in agreement with the pharmacokinetic data of pembrolizumab and nivolumab in the limited human studies that have assessed this metric^{21,22} (**Figure 2C, D**).

MC-38 mouse colon carcinoma tumors are sensitive to PD-1/L1 blockade therapy in preclinical models that use anti-mouse PD-1/L1 antibody clones^{15,23}. As a final step in the characterization of HuPD-H1 mice, we sought to determine if this was true when treating with FDA-approved therapies. We created MC-38huPD-L1 cells in which the mouse PD-L1 sequence was removed and replaced by the human PD-L1 sequence, thus making both the host and tumor cells a fully humanized PD-1/L1 system (**Figure 3A**). Following s.c. injection of MC-38huPD-L1, mice began receiving anti-human PD-1/L1 antibodies (i.p.) on day 7 of tumor growth (**Figure 3B**). As expected, treatment resulted in tumor growth inhibition in the majority of mice. Notably, there were two complete responders (CRs) with no evidence of tumors after treatment in the pembrolizumab group and two in the avelumab group, while avelumab treatment resulted in a significant increase in overall survival (**Figure 3C-E**). Thus, our humanized PD-1 and PD-L1 mouse model recapitulates the therapeutic effects of FDA-approved PD-1 or PD-L1 antibodies *in vivo*.

Direct comparison of the antitumor immune response generated by FDA-approved anti-PD-1/L1 antibodies in an in vivo T cell priming model

Recent evidence suggests that the antitumor effects of PD-1/L1 antibody therapies are transpiring in the periphery in connection with T cell priming^{11,12,13}. Thus, we sought to directly compare the strength of the immune response generated if each antibody was present at the time of T cell priming within our *in vivo* model. To do this, we intraperitoneally (i.p.) administered anti-PD-1/L1 antibody therapeutics during an initial T cell priming window against a surrogate tumor antigen (OVA). The treatment was then discontinued, and the strength and durability of the systemic T cell response was evaluated with a subcutaneous (s.c.) tumor challenge distant from the T cell priming site (**Figure 4A**).

Mice were treated with PBS, pembrolizumab, nivolumab, atezolizumab, or avelumab on days -1, 1, and 3, surrounding an immunization with OVA protein and poly I:C adjuvant on day 0 (**Figure 4A**). One week after immunization, mice were challenged with a s.c. injection of B16-OVA mouse melanoma tumor cells in the right flank (**Figure 4B**). The majority of mice in the PBS-treated group had visible tumors by day 6 posttumor injection (**Figure 4C-E**; black lines). In contrast, mice that were primed with OVA in the presence of anti-PD-1/L1 therapies displayed a much greater capacity to delay tumor formation or prevent it altogether. Interestingly, the two anti-PD-L1 therapies had the strongest effect, with 3/5 atezolizumab-treated mice and 5/5 avelumab-treated mice rejecting tumor formation out to day 19 post tumor injection (**Figure 4F**).

To test the durability of this protective antitumor response, we rechallenged all the mice that had no signs of primary tumor growth 3 weeks after tumor injection with a second injection of B16-OVA tumor cells at a distant site (this time on the left flank, **Figure 4G**). This rechallenge occurred a total of 4 weeks after the last drug treatment, precluding any effects from circulating antibody. The majority of the mice that were OVA-immunized in the presence of anti-PD-1/L1 blockade were able to reject a second tumor challenge at

a distant site, including all 5 of the mice initially primed with avelumab (**Figure 4H**). To determine whether this was an antigen-specific effect, we also challenged the mice with an injection of B16F10 (non-OVA expressing) tumor at a third location. The B16F10 tumors grew out in all mice (**Figure 4I**), indicating that the rejection of B16-OVA was due to an antigen-specific adaptive immune response. Collectively, these results show that FDA-approved anti-PD-1/L1 monoclonal antibody therapeutics modulate T cell priming to generate durable immunity against tumor formation and that these effects can be directly compared in the HuPD-H1 model.

Anti-PD-L1 antibody increases the expansion of antigen-primed, cytotoxic CD8⁺ T cells for protective immunity

In our *in vivo* model, all mice were primed with OVA and poly I:C to generate an antigen-specific CD8⁺ T cell response. We confirmed that OVA-specific CD8⁺ T cells were produced equivalently in both PBS- and anti-PD-1/L1-treated mice (**Supplemental Figure 2**). In both groups, this response peaked at day 7 after immunization, with decreasing amounts of OVA-tetramer⁺ CD8⁺ T cells over time. However, we found no significant difference in the abundance of OVA-specific tetramer⁺CD8⁺ cells between controls and drug-treated mice at any of the time points we assessed. Hence, despite the clear presence of antigen-specific cells within the PBS mice, these cells failed to prevent eventual tumor growth. This was in contrast to the mice primed in the presence of anti-PD-1/L1 (**Figure 4C-E**).

To explain this, we next considered whether treatment with FDA-approved therapies at the time of antigen stimulus led to a shift in the phenotype of the resulting T cells such that they were more *functionally* able to control tumor seeding and growth and whether this could account for the more effective and durable antitumor immunity within those mice. For these experiments, we focused on PBS control vs. avelumab-treated mice, as avelumab had the most robust effect in the previous *in vivo* challenge experiments. We isolated spleens from mice primed with avelumab (vs. PBS) and compared the phenotype and abundance of CD8⁺ T cells 72 hours after B16-OVA tumor injection (d10 overall) with a large panel of T cell markers via CyTOF (**Figure 5A; Supplemental Table 1**). We then performed viSNE dimensionality reduction analysis using equal numbers of CD3⁺CD8⁺ T cells as input and produced tSNE maps that distributed the cells based on their phenotype (level of marker expression). We noted an increased density of cells near the center of the map that was specific to the avelumab-treated mice (**Figure 5B**, pink arrows). The overlay of T cell marker expression onto the maps revealed that this subpopulation was CD44^{hi}CD62L^{lo} (effector T cells). They were also Ki67 positive, indicating proliferation at the time of tumor challenge. Furthermore, the cells were relatively high in PD-1 expression, with moderate expression of the transcription factor Eomes, indicating that they were differentiated and antigen-primed^{24, 25} (**Figure 5C**). They moderately expressed BATF, a transcription factor shown to counter T cell exhaustion²⁶. Conversely, the population of interest was relatively low in Tcf1 expression. Previously, PD-1⁺Tcf1^{lo} cells have been characterized as fully differentiated, effector T cells that are produced from Tcf1^{hi} cells and promote tumor control in response to ICB therapy²⁷. Finally, we noted that the subset of interest in the avelumab-treated mice displayed noticeably high expression of CD11a and CX3CR1 (**Figure 5C**).

Interestingly, the CD11a^{hi}CD8⁺ T cell population has been used previously as a surrogate for total antigen-primed T cells in both mice and humans²⁸. In addition, our group was the first to discover increased expression of the chemokine receptor CX3CR1 in the CD8⁺ T cells of successful responders to anti-PD-1 treatment²⁹. Since that time, the CX3CR1⁺CD8 T cell population has been found to increase in responders after treatment in a number of studies, including models of both tumor and chronic viral infection^{30, 31, 32, 33, 34}. Taken together, our results from the HuPD-H1 model show that expansion of this critical CX3CR1⁺CD8 T cell subset can be induced by the presence of ICB therapy at the time of T cell priming and indicate that these are the cells mediating the enhanced tumor rejection in the anti-PD-1/L1-treated mice.

To further verify these results, we completed an additional analysis of the CyTOF data using CITRUS, an algorithm that iteratively hierarchically clusters cells based on similarity of expression of subsets of the measured channels. This produced a map of nodes (a “tree”) with parent nodes upstream of their relative progeny (**Figure 5D**). Each node contains cells with similar phenotypes based on marker expression. Statistical analysis (FDR 5%) found that cluster (or node) #119994 was significantly more abundant in the avelumab-primed mice than in the controls (**Figure 5E**). Overlay of the relative expression of various markers onto the CITRUS map revealed that cluster #119994 had high expression of Ki67, PD-1, CD11a, and CX3CR1 (**Figure 5F**). This, therefore, represents the same population of therapy-responsive cells initially found via the tSNE maps.

To validate our CyTOF findings in an expanded number of samples, we used flow cytometry to show that mice primed in the presence of avelumab had significantly more CD11a^{hi} CX3CR1⁺PD-1⁺CD8⁺ cytotoxic T cells at day 10 post-OVA immunization than control mice (**Figure 5G**).

Finally, to confirm that tumor rejection induced by OVA/poly I:C plus avelumab was indeed a CD8⁺ T cell-dependent effect, we depleted CD8⁺ T cells starting on day -1 at the time of the first drug treatment. We found that mice primed against OVA, but without CD8⁺ T cells, were unable to reject the B16-OVA tumor challenge, even if priming took place in the presence of avelumab (**Figure 5H**). Collectively, our results indicate that ICB therapy at the time of T cell priming can induce expansion of a unique effector-like CD8⁺ T cell population capable of tumor rejection. This population correlates with tumor rejection both in our model and in patient clinical samples^{29, 35}.

Discussion

Although the current FDA-approved anti-PD-1 or PD-L1 blocking antibodies have demonstrated encouraging clinical responses, their underlying mechanisms of action still need to be better defined, particularly for optimizing therapeutic timing and identifying new opportunities for rational combination therapy. To that end, we successfully generated humanized PD-1 and PD-L1 mice in which the human sequences of the extracellular domains of PD-1 and PD-L1 were used to replace both mouse PD-1 and PD-L1. Unlike current preclinical models that utilize anti-mouse antibody surrogates or

immunocompromised mice with human-derived bone marrow, our HuPD-H1 mice allow direct comparison of FDA-approved anti-PD-1 and anti-PD-L1 therapeutics within fully immunocompetent C57BL/6 mice.

Although the ultimate safety and efficacy of immune checkpoint inhibitors are best defined in human clinical studies, preclinical models are still needed to understand the biological impacts of these therapies that cannot be easily identified from patient samples. For example, the use of CTLA-4 humanized mice³⁶ was essential for delineating the true mechanism of anti-CTLA-4 antibodies *in vivo*. Using the FDA-approved anti-CTLA-4 antibody that binds to human but not mouse protein, researchers were able to determine that binding of CTLA-4 efficiently induces Treg depletion and Fc receptor-dependent tumor rejection, rather than the previously accepted mechanism of blocking the interaction of B7 and CTLA-4. This observation not only explains why anti-CTLA-4 antibodies can cause severe colitis, which is usually controlled by Treg cells, but also provides a new platform for evaluating the next generation of therapeutic tools targeting CTLA-4 *in vivo*. Our humanized PD-1/L1 mouse model was created to serve a similar purpose in characterizing both current and future anti-PD-1/L1 therapeutics, including not only antibodies but also the novel small molecules being developed to target human PD-1/L1 signaling³⁷.

To date, there has been one previous study using a single knock-in humanized PD-1 mouse model³⁵. They showed that a nonblocking anti-PD-1 antibody could cause tumor regression *in vivo*, demonstrating a potential new avenue for the design of anti-PD-1 antibody therapeutics that do not necessarily block PD-1/PD-L1 interactions but can act through the CD28 costimulatory pathway. Although this single knock-in model yielded new insight, we considered evidence that the PD-1/PD-L1 pathway exhibits bidirectional signaling in the context of tumor-T cell interactions or other immune cell-T cell interactions^{38, 39, 40, 41}. Therefore, to best address the role of anti-human PD-1 or PD-L1 antibodies *in vivo*, we generated a model that incorporated both humanized PD-1 and PD-L1, ensuring the appropriate physiological ligation between the two molecules. Thus, by combining humanized PD-1 and PD-L1 in our HuPD-H1 mice, we now have a unique tool to address numerous questions surrounding these molecules and the therapies that target them. In the current manuscript, we focused on further delineating the biological impact of anti-human PD-1 or PD-L1 antibodies during T cell priming, a biological process that we know encompasses multiple levels of immune cell interactions engaging the PD-1 and PD-L1 signaling pathways^{42, 43, 44}. Our results demonstrate that FDA-approved anti-PD-1/L1 antibodies affect early T cell programming, resulting in a sustained effector T cell response capable of eliminating a subsequent tumor challenge. This highlights the potential of combining tumor vaccine therapy and anti-PD-1/PD-L1 antibodies to prevent tumor recurrence, which should be further explored in clinical trials.

Another advantage of our double humanized PD-1 and PD-L1 mice was its faithful recapitulation of the clinical relevance of CX3CR1⁺ CD8⁺ T cells in response to anti-PD-1 or PD-L1 therapy. We and others have previously reported that CX3CR1⁺ CD8⁺ T cells increase in the peripheral blood of responders to ICI therapy for patients with advanced melanoma or lung cancers^{29, 35}. However, it is still not clear how these PD-1 therapy-responsive CX3CR1⁺ CD8⁺ T cells are generated and expanded in patients. In this study, we

found that ICIs may expand CX3CR1⁺ CD8⁺ T cells shortly after T cell priming and that this subset of T cells shares many features of the effector memory phenotype (BATF⁺ and Eomes⁺TCF-1⁻). Interestingly, our study suggests that the *quality* of antigen-specific T cells rather than the quantity of antigen-specific T cells plays a critical role in response to ICI therapy, as all mice in our study, including controls, had a robust tumor-specific T cell immune response to the OVA antigen, but only in mice treated with ICI at the time of priming showed effective antitumor immunity.

Although the HuPD-H1 model is a promising new tool for use in advancing anti-PD-1/L1 science and therapeutic applications, biological differences between mice and humans will always be a limitation of preclinical studies. This is true, particularly with the accelerated timeline for tumor growth and treatment, which happens over only a few weeks in mice but over months and years in the clinical setting. In addition, we used the model antigen OVA in our studies along with a strong TLR-3 adjuvant, poly I:C. The effects of anti-PD-1/L1 therapies in combination with different strengths of antigen and various adjuvants will need to be tested across different tumor types to determine in what setting this combination is most effective for potential vaccine therapy. Finally, although we found increased levels of CX3CR1⁺PD-1⁺CD8⁺ effector T cell levels after priming in the presence of avelumab, we have not determined whether these cells are derived directly from the antigen-presenting cell/T cell interaction or from an event further downstream in T cell proliferation and expansion. The existence of “effector precursor” CD8⁺ T cells, initially primed in lymphoid tissues, that then proliferate and produce CX3CR1⁺CD8⁺ T cells upon treatment with PD-1 blockade is a possibility³¹. It will be important to use this new model to further parse the origin of CX3CR1⁺ cells, given their tight correlation with successful treatment response in humans.

In summary, our double humanized PD-1 and PD-L1 mice created on the immunocompetent C57BL/6 background provide an *in vivo* model to address the mechanisms of action of drugs aimed at human PD-1 or PD-L1. In the future, these mice will serve as a platform to evaluate rational combination treatments with chemotherapy, targeted small molecules, or radiation therapy, with the advantage that many syngeneic mouse tumor models have already been established on the C57BL/6 strain. In addition, the recapitulation of PD-1 therapy-responsive T cells in our model also suggests that future studies using these mice could reveal other immune cell biomarkers associated with and critical for the response to PD-1/PD-L1 inhibitors.

Declarations

Data Availability Statement

The datasets generated during the current study are available from the corresponding author upon request.

Funding

This work was supported by National Institute of Health grants R01 AI095239 and R01 CA256927.

(H. Dong) and R01 AR077518 (H. Zeng). W. Barham was supported by the Mayo Clinic Medical Scientist Training Program and by National Institute of Health Fellowship Award F30 CA250326. All diagrams were produced using Biorender.

Author Contributions (CRediT designations)

Conceptualization: WB and HD

Methodology: WB, MH, SMH, KDP, YY, ASM, HD

Formal Analysis: WB, MH, XZ, HZ, HD

Investigation: WB, MH, XL, SMH, JBH, JKG, XZ

Resources: HZ, ASM

Writing – Original Draft: WB and HD

Writing – Review & Editing: WB, MH, XL, SMH, JBH, JKG, XZ, HZ, KDP, YY, ASM, HD

Supervision: HD

Funding Acquisition: HD

Competing Interests

The authors have declared that no conflict of interest exists.

References

1. Vaddepally, R.K., Kharel, P., Pandey, R., Garje, R. & Chandra, A.B. Review of Indications of FDA-Approved Immune Checkpoint Inhibitors per NCCN Guidelines with the Level of Evidence. *Cancers (Basel)* **12** (2020).

2. Markham, A. Dostarlimab: First Approval. *Drugs* **81**, 1213-1219 (2021).
3. Passiglia, F. *et al.* Looking for the best immune-checkpoint inhibitor in pre-treated NSCLC patients: An indirect comparison between nivolumab, pembrolizumab and atezolizumab. *Int J Cancer* **142**, 1277-1284 (2018).
4. Fessas, P., Lee, H., Ikemizu, S. & Janowitz, T. A molecular and preclinical comparison of the PD-1-targeted T-cell checkpoint inhibitors nivolumab and pembrolizumab. *Semin Oncol* **44**, 136-140 (2017).
5. Lee, H.T. *et al.* Molecular mechanism of PD-1/PD-L1 blockade via anti-PD-L1 antibodies atezolizumab and durvalumab. *Sci Rep* **7**, 5532 (2017).
6. Donahue, R.N. *et al.* Analyses of the peripheral immunome following multiple administrations of avelumab, a human IgG1 anti-PD-L1 monoclonal antibody. *J Immunother Cancer* **5**, 20 (2017).
7. De Sousa Linhares, A. *et al.* Therapeutic PD-L1 antibodies are more effective than PD-1 antibodies in blocking PD-1/PD-L1 signaling. *Sci Rep* **9**, 11472 (2019).
8. Lepar, T. *et al.* Nivolumab to pembrolizumab switch induced a durable melanoma response: A case report. *Medicine (Baltimore)* **98**, e13804 (2019).
9. Feng, D. *et al.* Excellent Response to Atezolizumab After Clinically Defined Hyperprogression Upon Previous Treatment With Pembrolizumab in Metastatic Triple-Negative Breast Cancer: A Case Report and Review of the Literature. *Front Immunol* **12**, 608292 (2021).
10. Polesso, F. *et al.* PD-1-specific "Blocking" antibodies that deplete PD-1(+) T cells present an inconvenient variable in preclinical immunotherapy experiments. *Eur J Immunol* **51**, 1473-1481 (2021).

11. Wu, T.D. *et al.* Peripheral T cell expansion predicts tumour infiltration and clinical response. *Nature* **579**, 274-278 (2020).
12. Yost, K.E. *et al.* Clonal replacement of tumor-specific T cells following PD-1 blockade. *Nat Med* **25**, 1251-1259 (2019).
13. Zhang, J. *et al.* Compartmental Analysis of T-cell Clonal Dynamics as a Function of Pathologic Response to Neoadjuvant PD-1 Blockade in Resectable Non-Small Cell Lung Cancer. *Clin Cancer Res* **26**, 1327-1337 (2020).
14. Munder, P.G., Modolell, M. & Hoelzl Wallach, D.F. Cell propagation on films of polymeric fluorocarbon as a means to regulate pericellular pH and pO₂ in cultured monolayers. *FEBS Lett* **15**, 191-196 (1971).
15. Tang, H. *et al.* PD-L1 on host cells is essential for PD-L1 blockade-mediated tumor regression. *J Clin Invest* **128**, 580-588 (2018).
16. Dong, H. *et al.* Tumor-associated B7-H1 promotes T-cell apoptosis: a potential mechanism of immune evasion. *Nat Med* **8**, 793-800 (2002).
17. Tu, X. *et al.* PD-L1 (B7-H1) Competes with the RNA Exosome to Regulate the DNA Damage Response and Can Be Targeted to Sensitize to Radiation or Chemotherapy. *Mol Cell* **74**, 1215-1226 e1214 (2019).
18. Amir el, A.D. *et al.* viSNE enables visualization of high dimensional single-cell data and reveals phenotypic heterogeneity of leukemia. *Nat Biotechnol* **31**, 545-552 (2013).
19. Polikowsky, H.G. & Drake, K.A. Supervised Machine Learning with CITRUS for Single Cell Biomarker Discovery. *Methods Mol Biol* **1989**, 309-332 (2019).

20. Ben-Shaanan, T.L. *et al.* Activation of the reward system boosts innate and adaptive immunity. *Nat Med* **22**, 940-944 (2016).
21. Brahmer, J.R. *et al.* Phase I study of single-agent anti-programmed death-1 (MDX-1106) in refractory solid tumors: safety, clinical activity, pharmacodynamics, and immunologic correlates. *J Clin Oncol* **28**, 3167-3175 (2010).
22. Patnaik, A. *et al.* Phase I Study of Pembrolizumab (MK-3475; Anti-PD-1 Monoclonal Antibody) in Patients with Advanced Solid Tumors. *Clin Cancer Res* **21**, 4286-4293 (2015).
23. Lau, J. *et al.* Tumour and host cell PD-L1 is required to mediate suppression of anti-tumour immunity in mice. *Nat Commun* **8**, 14572 (2017).
24. Pearce, E.L. *et al.* Control of effector CD8+ T cell function by the transcription factor Eomesodermin. *Science* **302**, 1041-1043 (2003).
25. Goldberg, M.V. *et al.* Role of PD-1 and its ligand, B7-H1, in early fate decisions of CD8 T cells. *Blood* **110**, 186-192 (2007).
26. Seo, H. *et al.* BATF and IRF4 cooperate to counter exhaustion in tumor-infiltrating CAR T cells. *Nat Immunol* **22**, 983-995 (2021).
27. Siddiqui, I. *et al.* Intratumoral Tcf1(+)PD-1(+)CD8(+) T Cells with Stem-like Properties Promote Tumor Control in Response to Vaccination and Checkpoint Blockade Immunotherapy. *Immunity* **50**, 195-211 e110 (2019).
28. Liu, X. *et al.* Endogenous tumor-reactive CD8(+) T cells are differentiated effector cells expressing high levels of CD11a and PD-1 but are unable to control tumor growth. *Oncoimmunology* **2**, e23972

(2013).

29. Yan, Y. *et al.* CX3CR1 identifies PD-1 therapy-responsive CD8+ T cells that withstand chemotherapy during cancer chemoimmunotherapy. *JCI Insight* **3** (2018).
30. Zander, R. *et al.* CD4(+) T Cell Help Is Required for the Formation of a Cytolytic CD8(+) T Cell Subset that Protects against Chronic Infection and Cancer. *Immunity* **51**, 1028-1042 e1024 (2019).
31. Hudson, W.H. *et al.* Proliferating Transitory T Cells with an Effector-like Transcriptional Signature Emerge from PD-1(+) Stem-like CD8(+) T Cells during Chronic Infection. *Immunity* **51**, 1043-1058 e1044 (2019).
32. Ahrends, T. *et al.* CD4(+) T Cell Help Confers a Cytotoxic T Cell Effector Program Including Coinhibitory Receptor Downregulation and Increased Tissue Invasiveness. *Immunity* **47**, 848-861 e845 (2017).
33. Yamauchi, T. *et al.* Frequency of circulating CX3CR1+CD8+T cells to predict response to immune checkpoint inhibitor therapy. *Cancer Research* **80** (2020).
34. Yamauchi T, H.T., Oba T, Jain V, Chen H, Attwood K, Battaglia S, George S, Chatta G, Puzanov I, Morrison C, Odunsi K, Segal BH, Dy GK, Ernstoff MS, & Ito F T-cell CX3CR1 expression as a dynamic blood-based biomarker of response to immune checkpoint inhibitors. *Nature Communications* **12**, 1402 (2021).
35. Yamauchi, T. *et al.* T-cell CX3CR1 expression as a dynamic blood-based biomarker of response to immune checkpoint inhibitors. *Nat Commun* **12**, 1402 (2021).
36. Du, X. *et al.* A reappraisal of CTLA-4 checkpoint blockade in cancer immunotherapy. *Cell Res* **28**, 416-432 (2018).

37. Koblish, H.K. *et al.* Characterization of INCB086550: A Potent and Novel Small-Molecule PD-L1 Inhibitor. *Cancer Discov* **12**, 1482-1499 (2022).
38. Johnson, R.M.G., Wen, T. & Dong, H. Bidirectional signals of PD-L1 in T cells that fraternize with cancer cells. *Nat Immunol* **21**, 365-366 (2020).
39. Liu, X. *et al.* B7-H1 antibodies lose antitumor activity due to activation of p38 MAPK that leads to apoptosis of tumor-reactive CD8(+) T cells. *Sci Rep* **6**, 36722 (2016).
40. Lucas, E.D. *et al.* PD-L1 Reverse Signaling in Dermal Dendritic Cells Promotes Dendritic Cell Migration Required for Skin Immunity. *Cell Rep* **33**, 108258 (2020).
41. Kleffel, S. *et al.* Melanoma Cell-Intrinsic PD-1 Receptor Functions Promote Tumor Growth. *Cell* **162**, 1242-1256 (2015).
42. Gibbons, R.M. *et al.* B7-H1 signaling is integrated during CD8(+) T cell priming and restrains effector differentiation. *Cancer Immunol Immunother* **63**, 859-867 (2014).
43. Dammeijer, F. *et al.* The PD-1/PD-L1-Checkpoint Restrains T cell Immunity in Tumor-Draining Lymph Nodes. *Cancer Cell* **38**, 685-700 e688 (2020).
44. Oh, S.A. *et al.* PD-L1 expression by dendritic cells is a key regulator of T-cell immunity in cancer. *Nat Cancer* **1**, 681-691 (2020).

Figures

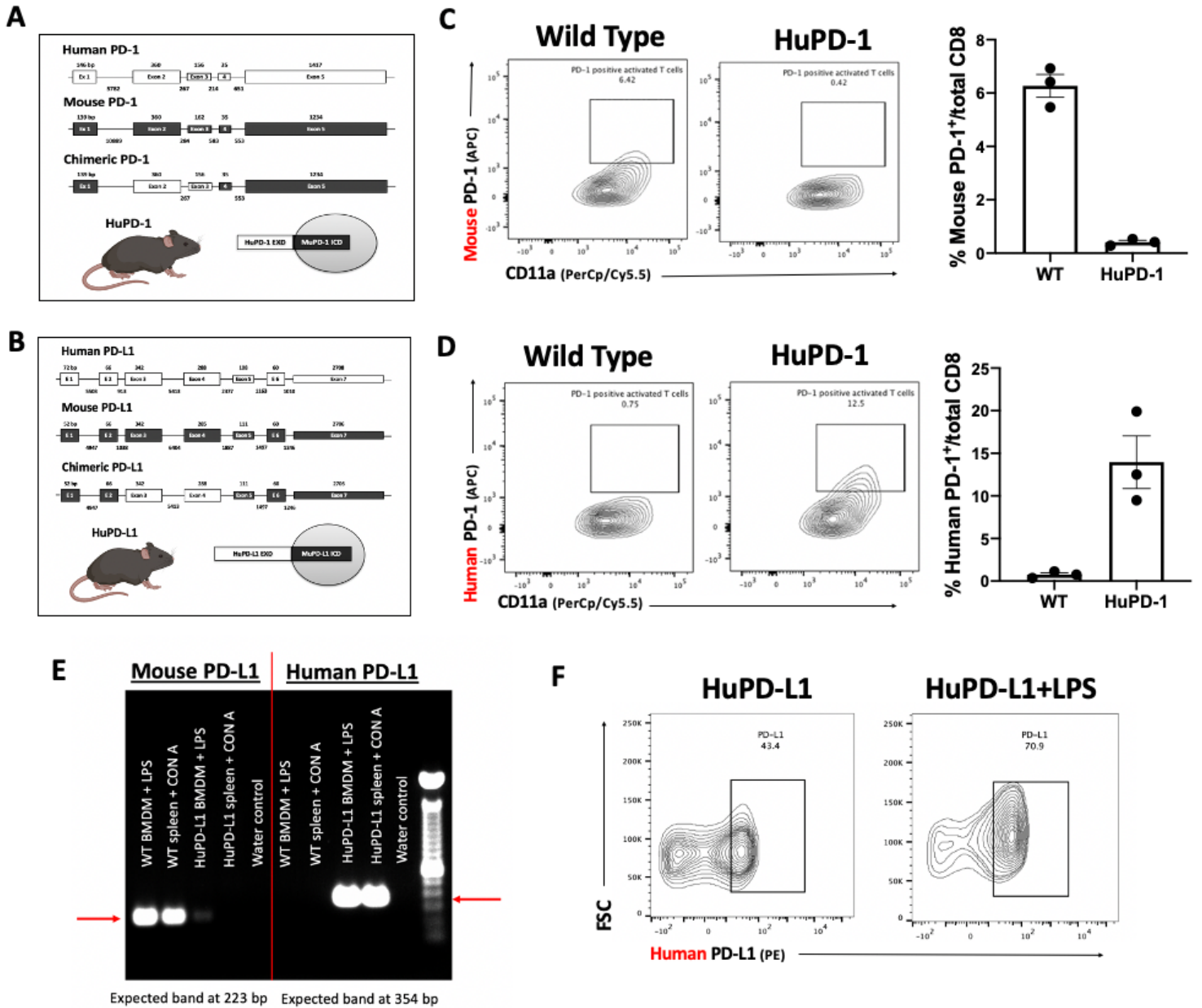


Figure 1

Generation and characterization of humanized PD-1 and PD-L1 mouse strains.

(A, B) Diagrams show the endogenous mouse exons coding for the extracellular domains of PD-1 (exons 2 and 3) or PD-L1 (exons 3 and 4) replaced with the coding sequence for the corresponding human exons to create two separate chimeric strains: HuPD-1 and HuPD-L1 (EXD, extracellular domain; ICD, intracellular domain). (C) Cells from the spleens of adult (3-4-month-old) C57BL/6 wild type mice or mice homozygous for the human PD-1 knock-in (HuPD-1) were plated and activated with anti-mouse CD3/CD28 beads for 48 hours followed by staining with commercial flow cytometry antibodies specific for either the mouse or human PD-1 sequence. Cells were first gated for CD8 positivity. Representative

flow plots show anti-mouse PD-1 antibody detecting PD-1 on wild type CD8⁺ T cells, quantified at right (n=3 mice per group; Bars, mean; error bars s.e.m.). (D) Anti-human PD-1 antibody detecting PD-1 on HuPD-1 CD8⁺ T cells, quantified at right (n=3 mice per group). (E) RT-PCR primers were designed to detect the mRNA sequences specific to the mouse or human PD-L1 extracellular domain. BMDM's and cells from the spleen of either WT or HuPD-L1 mice were treated with LPS or ConA to induce PD-L1 expression. RNA was isolated, and RT-PCR performed. Gel shows bands at expected sizes (red arrows). (F) Representative flow plots show human PD-L1 expression on the surface of BMDM's from HuPD-L1 mice and increased PD-L1 surface expression following treatment with LPS (FSC = forward scatter; bp = base pair).

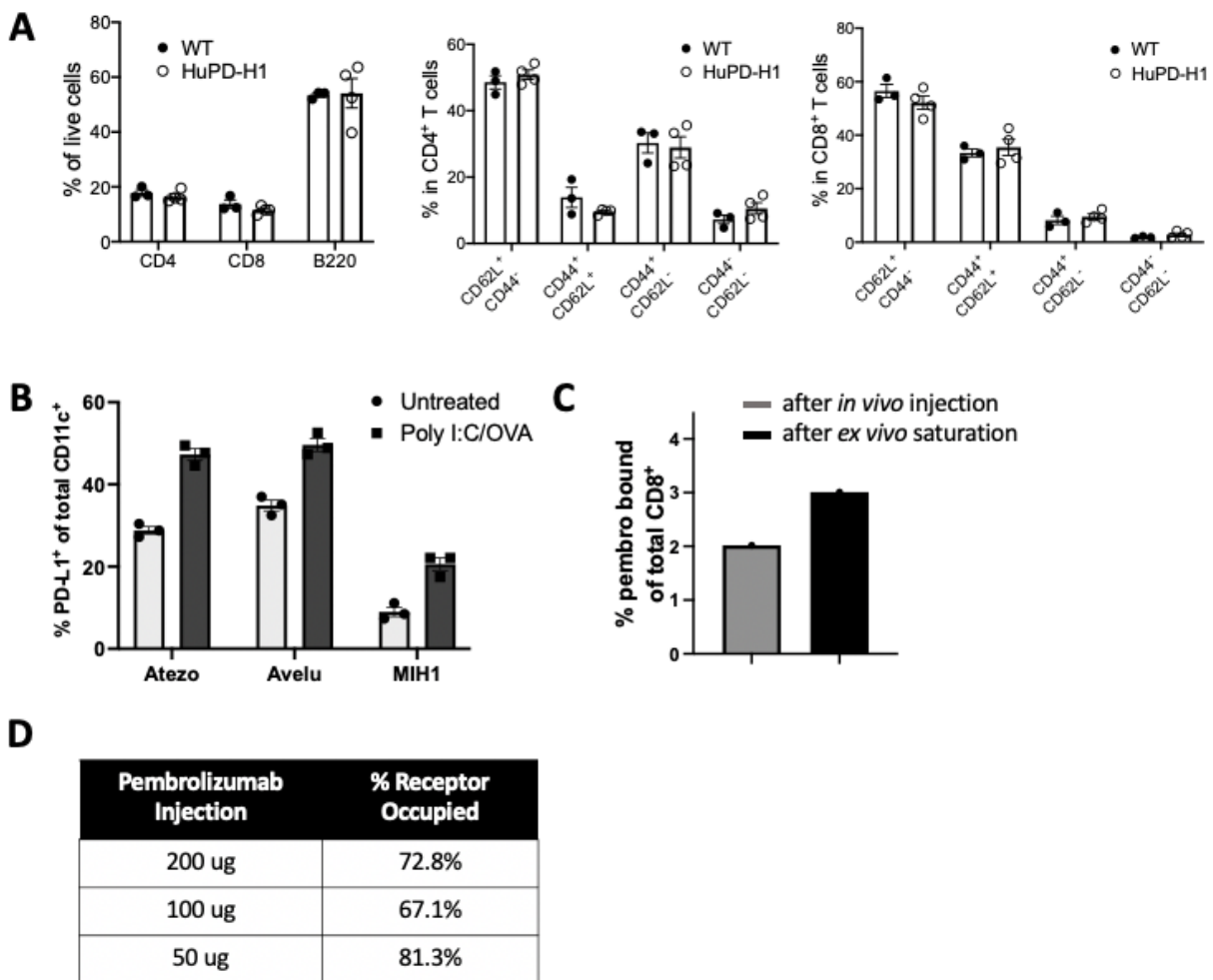


Figure 2

Immune profiling and evaluation of anti-human PD-1 and PD-L1 antibody binding in HuPD-H1 mice

(A) Splens of untreated HuPD-H1 mice and wild type (WT) C57BL/6 controls were analyzed via flow cytometry for T and B cell markers. No significant differences were found among the subsets (n=4 HuPD-H1, n=3 WT mice; Bars, mean; error bars s.e.m.). (B) DC's were isolated from the spleens of HuPD-H1 mice 20 hours after injection of OVA/poly I:C (vs. untreated mice). Atezo and Avelu were directly conjugated to AF647 and used to detect surface levels of human PD-L1 via flow cytometry vs. commercial anti-PD-L1 clone (M1H1); (n=3 mice/group; Bars, mean; error bars, s.e.m). (C) *In vivo* receptor occupancy of PD-1 by pembrolizumab. Gray bar is percent of total CD8⁺ T cells bound by pembrolizumab-AF647 24 hours after *in vivo* injection. Black bar represents percent of total CD8⁺ T cells from same mouse if saturated with pembrolizumab-AF647 *ex vivo*. The percent difference between these two values is the “receptor occupancy.” Bar graph is from 100 µg *in vivo* injection. Results from 3 different injection concentrations shown in (D) (n=3 mice).

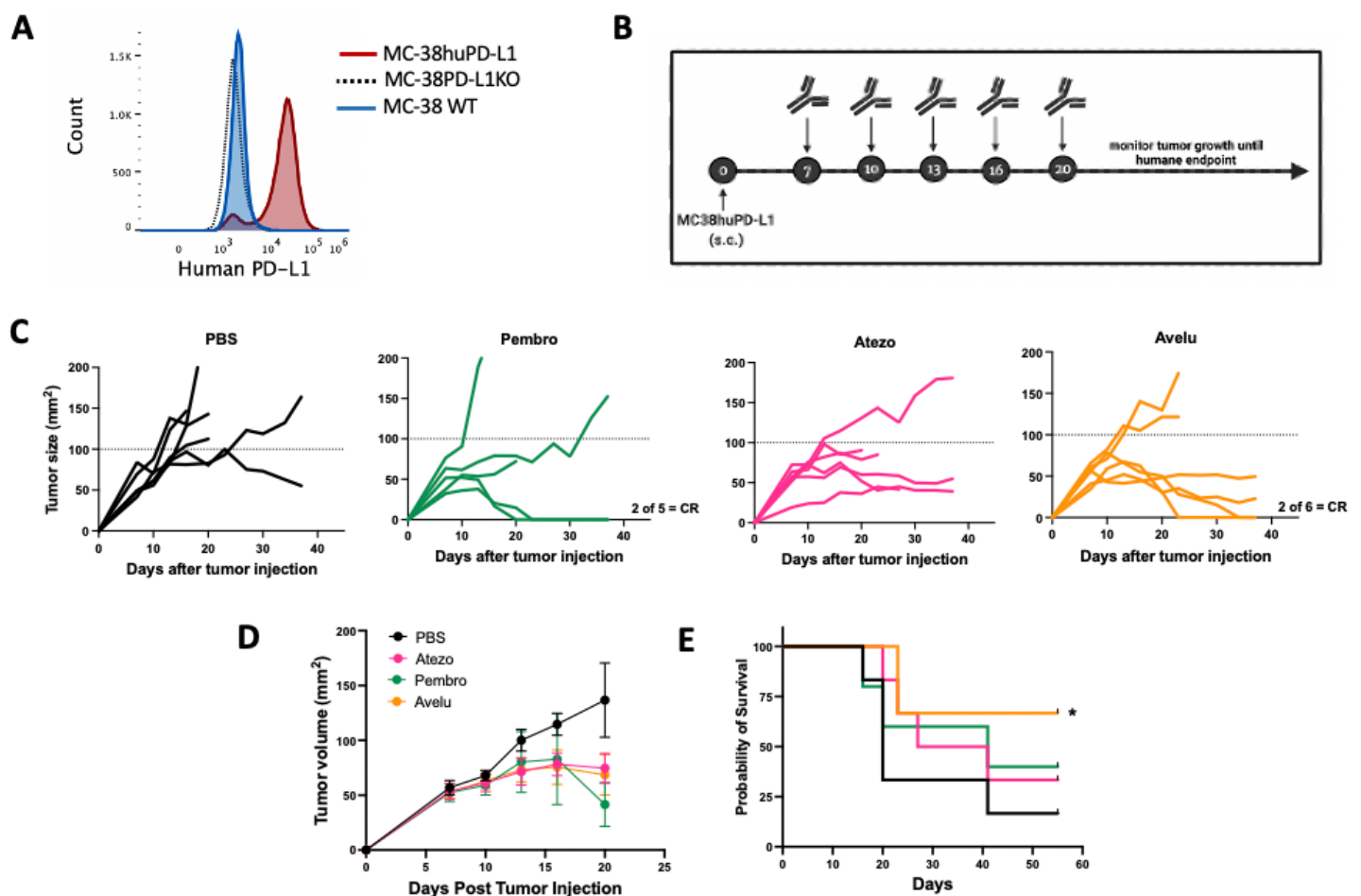


Figure 3

Therapeutic effects of FDA-approved anti-PD-1/L1 antibodies in HuPD-1-H1 mice.

(A) Human PD-L1 expression confirmed on MC-38huPD-L1 cells (M1H1 clone used for detection). (B) Schematic of experimental timeline. Antibody was injected (i.p.) at 100 ug per mouse at each time point. (C) Individual tumor growth curves (n=6 PBS, n=5 pembro, n=6 atezo, n=6 avelu). CR = complete responder. (D) Averaged tumor growth curves (dot is mean, error bars s.e.m.). (E) Survival curve (* P < 0.05 avelumab vs. PBS, Gehan-Breslow-Wilcoxon test). Data is representative of two independent experiments.

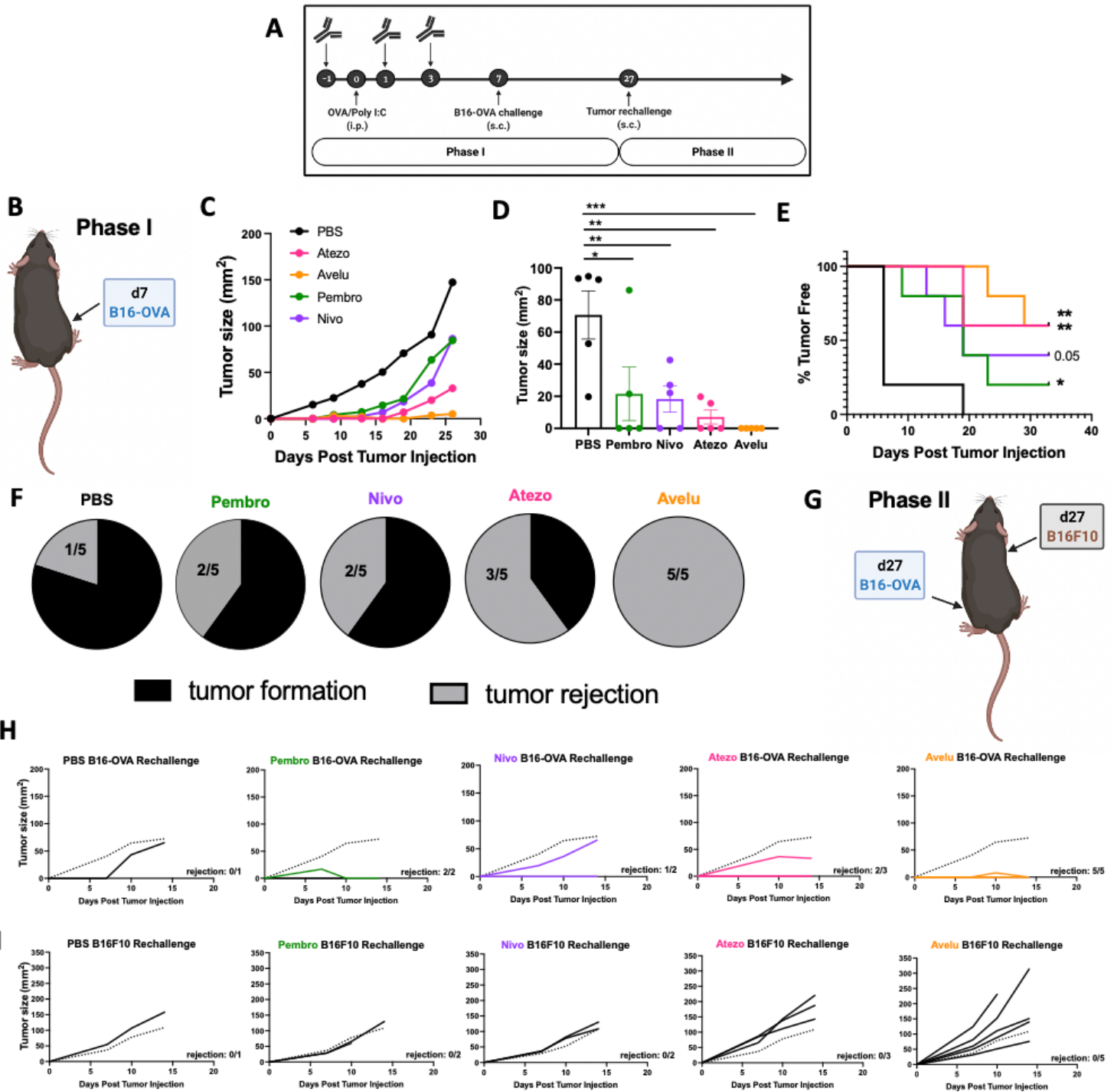


Figure 4

FDA-approved antibodies promote tumor antigen-specific vaccination therapy

(A) Schematic of two-phase experimental timeline. (B) Initial B16-OVA tumor injections were in right flank. (C) Averaged tumor growth curves of d7 B16-OVA tumors (n=5 mice per group, dot represents mean). (D) Tumor size comparison at day 19 of tumor growth (unpaired t test). Bars, mean; error bars, s.e.m. (**P < 0.01, *P < 0.05). (E) Time to tumor formation (each group compared to PBS, Log-rank (Mantel Cox) test). (F) Fraction of experimental mice (in C-E) that completely rejected d7 primary B16-OVA tumor challenge. (G) Mice without primary B16-OVA tumor growth were rechallenged at d27 with B16-OVA on the opposite (left) flank as well as B16F10 over the right shoulder. (H, I) Individual tumor growth curves for all rechallenged mice. Dotted line shows average growth of B16-OVA or B16F10 cells in completely naïve mice. All remaining mice were euthanized at day 14 after tumor rechallenge.

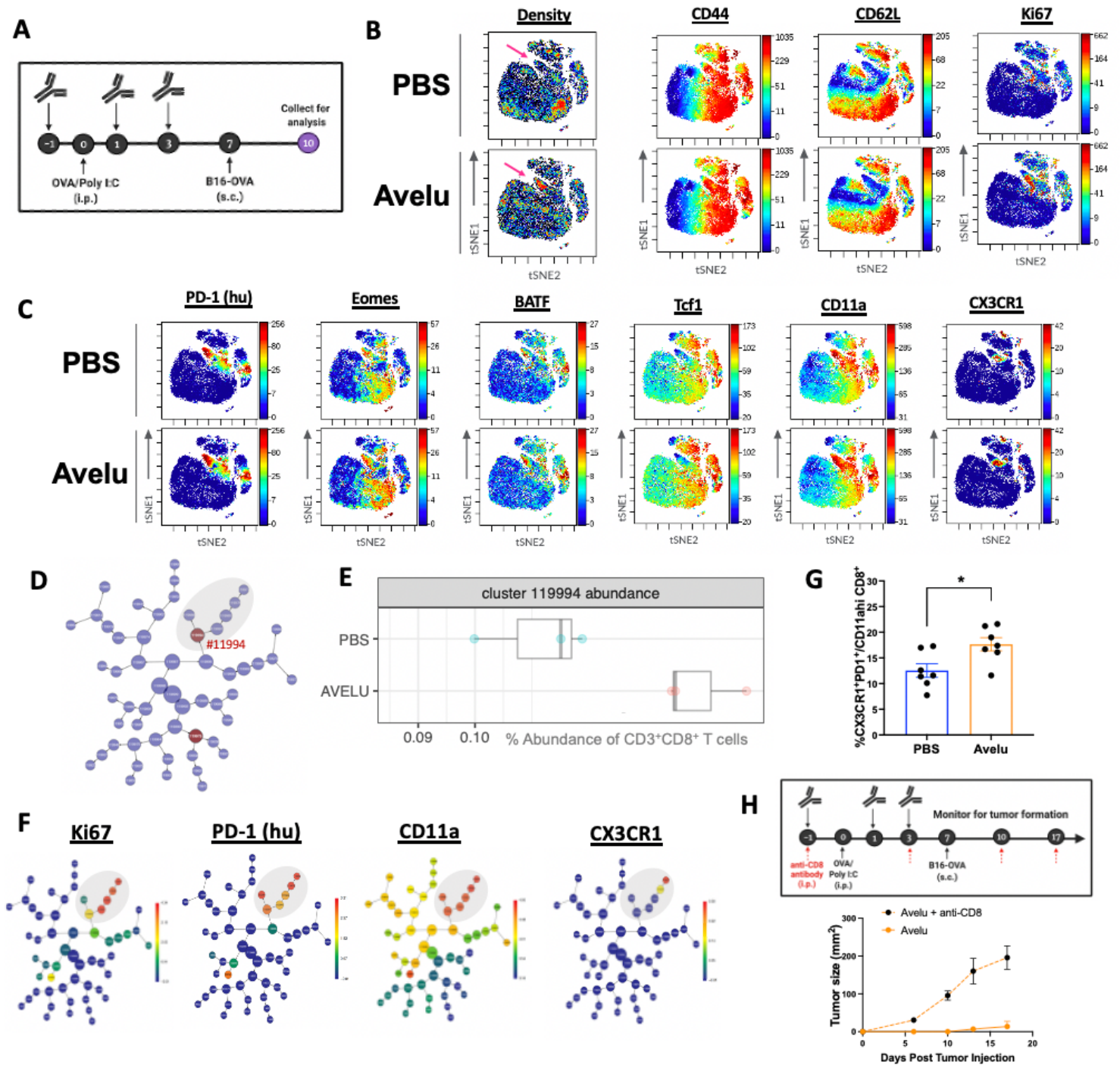


Figure 5

Anti-PD-L1 antibody increases the expansion of antigen-primed cytotoxic CD8⁺ T cells for protective immunity.

(A) Schematic of experimental timeline. (B, C) Cells isolated from spleens were assessed via CyTOF. High dimensional data was analyzed via Cytobank viSNE algorithm. CD3⁺CD8⁺ T cells from a representative PBS and avelumab sample are shown (n=3 PBS, n=3 avelumab total in analysis). Density

gradient indicates a population more prominent in the avelumab-treated mice (pink arrows). Additional plots display relative expression of various T cell markers. **(D)** CITRUS using SAM with a 5% FDR was completed to detect differences in the abundance of CD3⁺CD8⁺ T cell subsets in PBS vs. avelumab treated mice. Parent cluster #119994 (highlighted red, with progeny clusters shaded in gray) had a significantly higher abundance in avelumab-treated mice. **(E)** Cluster abundance shown as boxplot (n=3 CITRUS with SAM repeats produced similar results). **(F)** CITRUS clusters with expression of markers overlaid, indicates high expression (red) to low expression (blue) of each marker. Gray shading shows parent cluster #119994 and progeny, as in **D**. **(G)** Flow cytometry completed on separate samples (n= 7 mice/group, experimental timeline as in **A**). Bars, mean; error bars, s.e.m. (*P < 0.05). **(H)** *Above*, schematic of experimental timeline. *Below*, average tumor growth curves for each group (n=6 avelu; n=5 avelu + anti-CD8; dots, mean; error bars, s.e.m.).

Supplementary Files

This is a list of supplementary files associated with this preprint. Click to download.

- [SupplementalFigure1.png](#)
- [SupplementalFigure2.png](#)
- [SupplementalTable1.png](#)